Journal of Magnetic Resonance 307 (2019) 106570

Contents lists available at ScienceDirect

Journal of Magnetic Resonance

journal homepage: www.elsevier.com/locate/jmr

Single-shot velocity mapping by rewinding of velocity encoding with Echo-Planar Imaging

María R. Serial [a,b], Emilia V. Silletta [a,b], Josefina Perlo [c], Juan P. Giovacchini [a,b], Manuel I. Velasco [a,b], Bernhard Blümich [d], Ernesto D. Danieli [c], Federico Casanova [c], Rodolfo H. Acosta [a,b,*]

[a] Facultad de Matemática, Astronomía, Física y Computación, Universidad Nacional de Córdoba, Medina Allende s/n, X5000HUA Córdoba, Argentina
[b] Instituto de Física Enrique Gaviola (IFEG), CONICET, Medina Allende s/n, X5000HUA Córdoba, Argentina
[c] Magritek GmbH, Philipsstrasse 8, 52068 Aachen, Germany
[d] Institut für Technische und Makromolekulare Chemie, RWTH Aachen University, Worringerweg 2, 52062 Aachen, Germany

ARTICLE INFO

Article history:
Received 5 June 2019
Revised 5 August 2019
Accepted 7 August 2019
Available online 8 August 2019

Keywords:
Single-shot MRI
FLIESSEN-EPI
Velocity-encoded MRI
Kinematic viscosity
Couette cell

ABSTRACT

The ability of single-shot NMR imaging methods to follow the time evolution of a velocity distribution within an object is strongly limited by the phase errors accumulated as velocity maps are acquired. In the particular case of Carr-Purcell based sequences combined with Echo Planar Imaging acquisition, phase accumulates through subsequent images, hampering the possibility to acquire several velocity maps, which would be useful to determine transient behavior. In this work, we propose the use of a rewinding velocity encoding module applied after the acquisition of each image during the CPMG echo train. In this way, the first velocity module imparts a velocity dependent phase prior to the image acquisition and the second pair cancels this phase out before the next refocusing radiofrequency pulse is applied. The performance and limits of this method are studied by acquiring 100 images of a co-rotating Couette cell over a period of 1.6 s as a function of the rotation speed. The method is applied to determine the kinematic viscosity of a water/alcohol mixture, which is a relevant topic in many physical, chemical and biological processes.

1. Introduction

Magnetic resonance imaging (MRI) is a well-established method capable of measuring fluid motion in complex systems, such as those commonly found in medicine, biology, and engineering [1,2]. MRI is able to obtain spatially resolved velocity information in clear or opaque systems in a non-invasive way without the need for optical access as in laser Doppler anemometry [3] or the use of tracer particles as in particle imaging velocimetry [4]. One of the drawbacks of MRI velocimetry is its relatively low time resolution compared with other velocimetry techniques [5–7]. This represents an important limitation when studying non-stationary systems with transient behavior. In the past years, great effort has been put into the development and optimization of fast MRI velocimetry techniques in order to reduce the required acquisition time and increase the accuracy of the methods to measure velocity [8–13]. Perhaps the fastest velocity imaging sequence yet introduced relies on the use of fast low angle shot trains with sparse acquisition and compressed sensing reconstruction. By using fresh magnetization on each echo, individual velocity-encoded images can be acquired [14].

Most NMR velocimetry techniques combine a velocity encoding preparation period consisting of a pair of bipolar gradient pulses with a subsequent MRI acquisition module, where either a fast or a regular imaging technique can be employed, depending on the system under study [15,16]. From the available imaging sequences, Echo Planar Imaging (EPI) is one of the fastest techniques [17,18]. It was used for the first time to measure velocities in one direction by Firmin et al. [16]. Later, Kose proposed a method based on the acquisition of two consecutive EPI images to visualize turbulent flow and vortices in rotating samples [19] and circular pipes [20,21]. In order to measure two velocity components in the imaged plane in a one-shot experiment, Kose generated two spin echoes in the same excitation sequence and acquired one EPI image from each echo. By applying velocity gradients with different amplitudes along two perpendicular directions before the acquisition of each image, a phase shift proportional to the pixel velocity and the gradient amplitudes was defined for each image. By solving a set of two coupled equations, the two components of the velocity in each pixel were determined. Additionally, the magnitude of the image was shown to provide information on

* Corresponding author.
E-mail address: racosta@famaf.unc.edu.ar (R.H. Acosta).

https://doi.org/10.1016/j.jmr.2019.106570
1090-7807/

shear because of the signal loss due to a velocity distribution in each voxel [22,23].

A method suitable to determine the three velocity components using EPI was first introduced by Sederman et al. [24]. The so-called Gradient Echo Rapid Velocity and Acceleration Imaging sequence (GERVAIS) uses a train of 180° radiofrequency (rf) pulses to generate multiple echoes and acquires one image per echo. To determine the three velocity components, three images were acquired by applying velocity gradients along each direction prior to each image without phase rewinding after the image. Thus, the phase accumulated by previous images was subtracted mathematically. Additionally, the method requires a zero-flow image to be used as a reference image necessary to eliminate the systematic phase introduced by the imaging gradients. The method was later improved by acquiring a total of five images to generate a 3D velocity map. The so-called single-shot-GERVAIS (ss-GERVAIS) sequence [25] acquires two images during the first two echoes without applying velocity gradients so as to generate two reference images that account for the phases introduced by the even-odd behavior in the CPMG sequence. Velocity gradients are applied prior to the acquisition of the last three images without rewinding gradients, just as in the standard GERVAIS sequence. In order to produce a three-component velocity map from a single-shot experiment, the velocity phase shifts accumulated during the pulse sequence are mathematically treated during data post-processing to extract each individual velocity component. With this scheme, the flow field within a mobile droplet of oil was determined as it rose through a column of water.

As ss-GERVAIS needs less than 100 ms to produce a full 3-component velocity map and the echo trains can last longer than a second (depending on T_2), one could in principle measure a series of 3D maps from the same CPMG echo train. However, the fact that velocity gradients are not rewound before the generation of the next echo, gives rise to severe signal attenuation of images measured during the same echo train. This is so because the molecules contained inside each pixel have a small velocity distribution that generates a phase dispersion when successive velocity maps are collected. Additionally, in a general case, this velocity distribution enhances the phase dispersion via molecules migrating between pixels during the train. The absence of velocity-gradient rewinding also causes signal loss due to B_1 inhomogeneity. Moreover, the loss of magnetization determined by the inability of the rf pulses to refocus the B_0 inhomogeneity also affects the signal amplitude in the images. A similar situation was observed for sequences based on the RARE (Rapid Acquisition with Relaxation Enhancement) imaging module [26]. In this case, an alternative approach was introduced by Amar et al. [12], with the implementation of the Flow Imaging Employing Single-Shot Encoding (FLIESSEN) sequence, which accomplishes considerably higher tolerance to the maximum acceleration than a single-shot RARE sequence. This improvement was achieved by including rewinding velocity gradients after the acquisition of each echo. By updating the velocity information in each echo, a three-component velocity map of a levitating toluene drop was acquired in a single excitation experiment. Following the same principle, we present in this work a modified EPI velocimetry sequence where the velocity phase shift imparted by the velocity gradients applied before the image acquisition is removed immediately after it. This improvement to the standard EPI sequence enables studies of transient states as long as the system has long T_2. We refer to this new technique as FLIESSEN-EPI.

A velocity imaging method able to acquire a series of velocity maps is expected to find applications in the study of a non-stationary process. Additionally, it can be combined with rheological measurements to determine, for instance, shear banding instabilities [27]. For example, by measuring the velocity slow-down dynamics in a liquid system, the viscosity can be determined. When dealing with complex systems such as binary or micellar systems, viscosity renders useful information about the interactions of the mixture components on a molecular level. The viscosity of binary mixtures of water/alcohol has been thoroughly studied in the past [28–34] due to their wide range of applications, including fuel-cell technology, as solvents in industrial, environmental and pharmaceutical processes, and as model systems in bioscience among others. Due to the heterogeneity of the mixture at a molecular level, these solutions exhibit anomalous transport behavior. For example, it has been observed that the viscosity of water/alcohol mixtures assumes a maximum with a corresponding minimum for the diffusion coefficient for a particular composition [35]. This is due to hydration shells of water molecules surrounding the alcohol molecules, leading to the formation of clusters formed by hydrogen bonds [36,37].

In this work, we apply the new FLIESSEN-EPI sequence to measure the slow-down transient velocities of a water/alcohol mixture rotating in a Couette cell. The sequence was applied to acquire 100 images during a single excitation. The accuracy of the method to produce 20 three-component velocity maps reconstructed during this single-shot experiment was first tested using a phantom. Finally, the method was applied to determine the kinematic viscosity of a water/alcohol mixture as a proof-of-concept.

2. Materials and methods

2.1. Magnetic resonance imaging: The FLIESSEN-EPI sequence

EPI schemes rely on the generation of a train of gradient echoes by reversing the sign of the read gradient pulses and sampling the phase direction from negative to positive values in a sequential way. By combining it with a velocity-encoding module applied prior to the imaging period, EPI has proven to be one of the fastest velocity imaging sequences with great performance to study transient states of rapidly changing systems. Fig. 1a shows the ss-GERVAIS pulse sequence [25]. To encode the three orthogonal velocity components, a block of five images is required [26]. The first two images are acquired for reference (without velocity gradients) for odd and even echoes, respectively, and velocity-gradient pulses are applied subsequently during the last three images (for the sake of simplicity Fig. 1a shows only the first three). To enable the measurement of transient velocities, this block of five images needs to be applied repetitively in a CPMG pulse sequence where enough echoes can be generated to accommodate a large number of images. Fig. 1b shows a scheme of FLIESSEN-EPI, where an extra pair of bipolar gradients is applied after each image acquisition. As the polarity of the second pair of velocity-gradient pulses is reversed, the phase spread proportional to the velocity of the spins imparted by the first pair applied before the imaging module is simply removed before the next 180° pulse. However, if the particle velocity varies with time, as is the case with particles in circular motion, a phase shift proportional to their acceleration is accumulated and passed on to the next image.

The experiments presented in this work were carried out at 7.05 T field strength in an Oxford superconducting magnet operated with a Kea2 (Magritek GmbH) console. A 3D gradient coil system (Bruker GmbH) with a maximum gradient of 1.5 T/m was powered by a set of two dual channel Techron LVC5050 audio amplifiers. To excite and detect the NMR signal a 25 mm inner diameter birdcage rf coil and a 100 W Tomco radiofrequency amplifier were used. For all imaging experiments, the field of view was set to 25×25 mm^2 and matrices of 32×16 points were collected, defining a resolution of 780×1560 μm^2 per pixel. Velocity

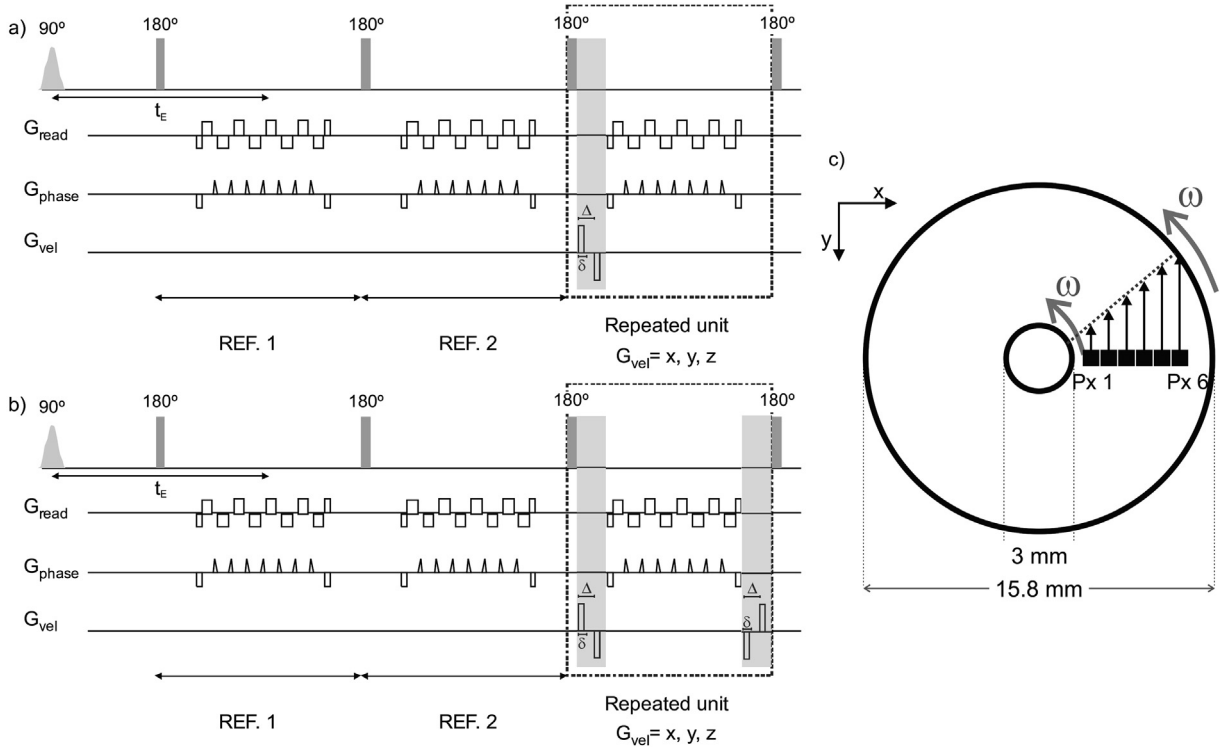

Fig. 1. (a) Modified ss-GERVAIS and (b) FLIESSEN-EPI pulse sequence schemes. The box indicates the number of repeated images, which is three in the case of three-component velocity encoding. This block of five echoes may be repeated in order to determine transient velocities. (c) Schematic representation of the co-rotating Couette cell used in the experiments. Both cylinders rotate at the same frequency.

was encoded with bipolar gradient pulses of δ = 1 ms duration and with an observation time of Δ = 1.2 ms.

The steady-state and the transient behavior of distilled water inside a co-rotating Couette cell were studied. Additionally, the FLIESSEN-EPI technique was applied to describe the transient velocities of a 52.7% mol 2-propanol aqueous solution. The employed echo time for the water sample was 16 ms, leading to a total acquisition time of 80 ms to obtain a three-component velocity map. In the case of the 2-propanol aqueous solution, a frequency selective pulse of 3 ms duration was used to detect water protons only, and an echo time of t_E = 18 ms was employed.

2.2. Couette cell

Stationary and transient flow were studied in a custom build co-rotating Couette cell, see Fig. 1c. Both concentric cylinders were made of acrylic, with the cell's inner and outer radii being r_i = 1.5 mm and r_o = 7.9 mm, respectively. A home-made rotation transmission system was employed. The cell rotation is driven by a 0.5 HP triphasic engine whose rotational frequency and acceleration rates were controlled by a Sinamics G110 frequency inverter (Siemens) that can be either manually or remotely operated [38]. For transient flow experiments, the frequency inverter was triggered with a TTL signal from the NMR console, thus being synchronized with the MRI acquisition. The engine was located in a room adjacent to the superconducting magnet, and a horizontal drive shaft made of aluminum was connected to a vertical shaft that was attached to the Couette cell by a flexible steel cord. The main reason to use a co-rotating Couette cell is that no instabilities are generated when both cylinders rotate at the same angular velocity, independent of the flow's Reynolds Number [39], giving a linear pattern of velocities as a function of the radius, $v(r) = \omega r$. This makes it an ideal phantom to test the performance of new velocity-encoding sequences in a wide range of angular velocities. For transient flow experiments, an acceleration of 1 rps/s and deceleration of 3.3 rps/s was employed for the start-up and the shut-down of rotations, respectively.

2.3. NMR simulations

NMR simulations were performed in MATLAB 2012b in order to examine movement related errors in the velocity maps obtained with the FLIESSEN-EPI sequence. The sample was rasterized using a 2D cylindrical grid, where each element was considered as a volume element with an associated magnetization vector. The total NMR signal at the echo maxima was then obtained by summation over all the grid points.

The program follows the magnetization evolution of each element of the grid during the application of the pulse sequence. In the rotating frame and with the detection frequency set on resonance, the magnetization vector of a volume element evolves under the influence of a magnetic field gradient $\boldsymbol{G}$, according to the following expression [1]:

$$M_+(\boldsymbol{r}, t) = M_+(\boldsymbol{r}, 0)e^{-i\gamma \boldsymbol{r}\ \boldsymbol{G}t},$$

where γ is the gyromagnetic ratio, $M_+ = M_x + iM_y$ is the transverse component of the total magnetization, $\boldsymbol{r}$ is the volume element position, and t is the time during which the gradient is applied. Relaxation was included in calculations by means of exponential decays in the magnetization evolution. During the application of pulsed gradients and sequence time delays, the position of each volume element was constantly updated according to the fluid dynamics of the system, in this case, the tangential velocity of spins was set to be proportional to the angular velocity.

Even though rf pulses were considered to be perfect rotations of the magnetization vector, two references, and three velocity-encoded images were recorded for all simulations, in order to com-

pare the obtained results with experimental data. The relaxation time T_2 was set to 2 s to match the experimental conditions, and the same timings as those used in the experiments were employed. Longitudinal relaxation was not considered since all experiments start from equilibrium conditions. Phase cycling schemes were not applied as all experiments presented are single-shot measurements.

2.4. Computational fluid dynamics

Experimental results are contrasted with CFD calculations, from which the viscosity of the system can be determined. The numerical results were obtained by solving the lattice Boltzmann equation (LBE) [40–42], a particular phase-space and temporal discretization of the Boltzmann equation (BE) [43,44]. The BE governs the time evolution of the single-particle distribution function $f(\mathbf{x}, \xi, \mathbf{t})$ where $\mathbf{x}$ and ξ are position and velocity in phase space. In LBE, the variable $\mathbf{x}$ is discretized and takes values on a uniform grid (the lattice), while ξ is not only discretized but also restricted to a finite number Q of values [40]. In an isothermal situation and in the absence of external forces, like gravity, the LB*E* can be written as:

$$f(\boldsymbol{x} + \mathbf{c_i}\delta t, t + \delta t) = f_i(\boldsymbol{x}, t) + \Omega_{ij}\left(f_j(\boldsymbol{x}, t) - f_j^{\mathrm{eq}}(x, t)\right), \quad i,j = 0, 1, \cdots, Q-1. \tag{1}$$

Here $f_i = f_i(\boldsymbol{x}, t)$ is the i-th component of the discretized distribution function at the lattice site $\boldsymbol{x}$, time t, and discrete velocity$\boldsymbol{c}_i$. The function $f_j^{\mathrm{eq}}(\boldsymbol{x}, t)$is a discrete version of the equilibrium distribution function [40] and $\boldsymbol{\Omega}$ is a linearized collision operator. In our simulations, we use an MRT model (Multiple Relaxation Times) [45,46]. In this case, $\boldsymbol{\Omega}$ can be written as $\Omega = -\mathbf{M}^{-1}\mathbf{S}\mathbf{M}$, with $\boldsymbol{S}$ a diagonal relaxation matrix. The so-called moments are defined by $|m(\boldsymbol{x}, t) > \equiv \mathbf{M}|f(\boldsymbol{x}, t) >$. In these new variables, the Eq. (1) becomes:

$$m(\boldsymbol{x} + \boldsymbol{c}\delta t,\ t + \delta t) >= |m(\boldsymbol{x}, t) > + \boldsymbol{S}(|m(\boldsymbol{x}, t) > - |m^{\mathrm{eq}}(\boldsymbol{x}, t) > \tag{2}$$

A time step in lattice Boltzmann methods (LBM) is typically divided into two parts, local collision, and the streaming process. If LBM-MRT is used, the collision is carried out using the moments, with Eq. (2), while the streaming is carried out using Eq. (1). At each time step, the macroscopic variables are recovered as:

$$\rho(\boldsymbol{x}, t) = \sum_{i=0}^{Q-1} f_i(\mathbf{x}, t), \quad \rho\boldsymbol{u}(\boldsymbol{x}, t) = \sum_{i=0}^{Q-1} \boldsymbol{c_i} f_i(\boldsymbol{x}, t), \tag{3}$$

where $\rho(\boldsymbol{x}, t)$ and $\rho\boldsymbol{u}(\boldsymbol{x}, t)$ are, respectively, the macroscopic fluid density and momentum.

In this work, the numerical result is obtained using a quasi-incompressible D3Q19 LBM_MRT model (three-dimensional $D = 3$ and $Q = 19$ discrete velocities). The model parameters, such as relaxation times in $\boldsymbol{S}$, transformation matrix $\boldsymbol{M}$, and equilibrium moments $m^{\mathrm{eq}}(\boldsymbol{x}, t)$ have been selected following those in [45]. The boundary conditions on the cavity boundary are imposed by applying a method known as bounce-back [47]. The bounce-back boundary condition allows us to set the spatial and temporal boundary velocity profile to represent the cavity walls' rotation. To simulate the fluid problem, we use 100 lattice points along the cavity diameter, and 402 lattice points along the cavity major axis.

3. Results and discussion

3.1. Comparison between ss-GERVAIS and FLIESSEN-EPI

In order to study the efficiency of FLIESSEN-EPI on the phase accumulation during a train of pulses, 100 images were acquired in the co-rotating Couette cell filled with distilled water, where 20 three-component velocity maps can be calculated. The results from the FLIESSEN-EPI sequence are compared to the data acquired with ss-GERVAIS by using the same sequence timings. That is, instead of placing the velocity encoding gradient pulses around the 180° rf pulses as in the original publication, we use a pair of bipolar pulses prior to image acquisition in each echo. While the original ss-GERVAIS would require a slightly shorter echo time a negligible effect was observed. Fig. 2a shows the first and last images acquired with a CPMG sequence from the static cell. The normalized intensity evolutions of different regions of interest are shown in Fig. 2b, corresponding to pixels close to the inner cylinder (Px 1), the central region (Px 3) and the outer cylinder (Px 6). The performance of both sequences is very similar. The limiting factor is transverse relaxation, if for instance toluene was used, longer echo trains could be acquired.

When the cylindric cell rotates at 2 rps, the images produced with the ss-GERVAIS sequence become seriously degraded as the image number increases, while no appreciable distortions are observed for FLIESSEN-EPI (see Fig. 2c). Fig. 2d shows the intensity of Px 1, Px 3 and Px 6 where it can be observed that for FLIESSEN-EPI the intensity of the last image decreases only from ca. 0.4 to 0.35. On the other hand, the echo train for ss-GERVAIS starts to degrade as of image number 10, which is clearly observed in the intensity drop of Px 6. The presence of the oscillation is due to uncompensated phases during the echo train. A period of 16 images is observed, which for this rotation speed corresponds to half of a complete turn. It must be pointed out that even for long echo trains, the signal is still above the noise level (0.1 compared to 0.005). The dependence of the signal loss with the velocity is more clearly observed in Fig. 3, where the image intensity is plotted for seven pixels equally distributed along the x-axis going from the inner cylinder to the outer one at four times during the echo train. For the first echo (t_E = 16 ms) both pulse sequences show similar signal intensities under static or rotating conditions, however, as the echo number increases, the signal amplitudes on the images produced by the ss-GERVAIS get more and more attenuated compared with the intensities on the images produced with the FLIESSEN-EPI. This signal loss gets more pronounced for pixels at larger radii, where the velocities are higher.

3.2. Errors in the velocity encoding

One of the main questions addressing the performance of the sequence refers to the errors expected in velocity determinations with FLIESSEN-EPI. To answer this question, we first center our attention on the performance of the sequence as a function of the rotation rates for a single block of 5 images. Fig. 4a shows maps of the velocity components along the x, y and z directions for the water-filled Couette cell where inner and outer cylinders rotate at 2 rps. To ensure a steady-state rotation, the sample was set in movement 5 min before performing the measurement. The velocities along the x and y directions depend linearly on the spatial coordinates, while small velocities along the axial direction are observed, as expected. The obtained minimum and maximum velocities in the x-y plane (19.2 mm/s – 98.1 mm/s) agree within 1% with the expected values determined by the cell dimensions. It is worth mentioning that the results shown in Fig. 4 are obtained in a single-shot experiment with a total experimental time of 80 ms. Fig. 4b shows the 1D velocity profiles along the x-axis of the V_y maps. The rotation frequency calculated from the slope of the data shown in Fig. 4b agrees with the expected value for three different rotation speeds, as shown in Fig. 4c. The velocity of the fluid between the inner and outer walls is measured with good accuracy for 8 pixels even when the pixels closest to the cell wall

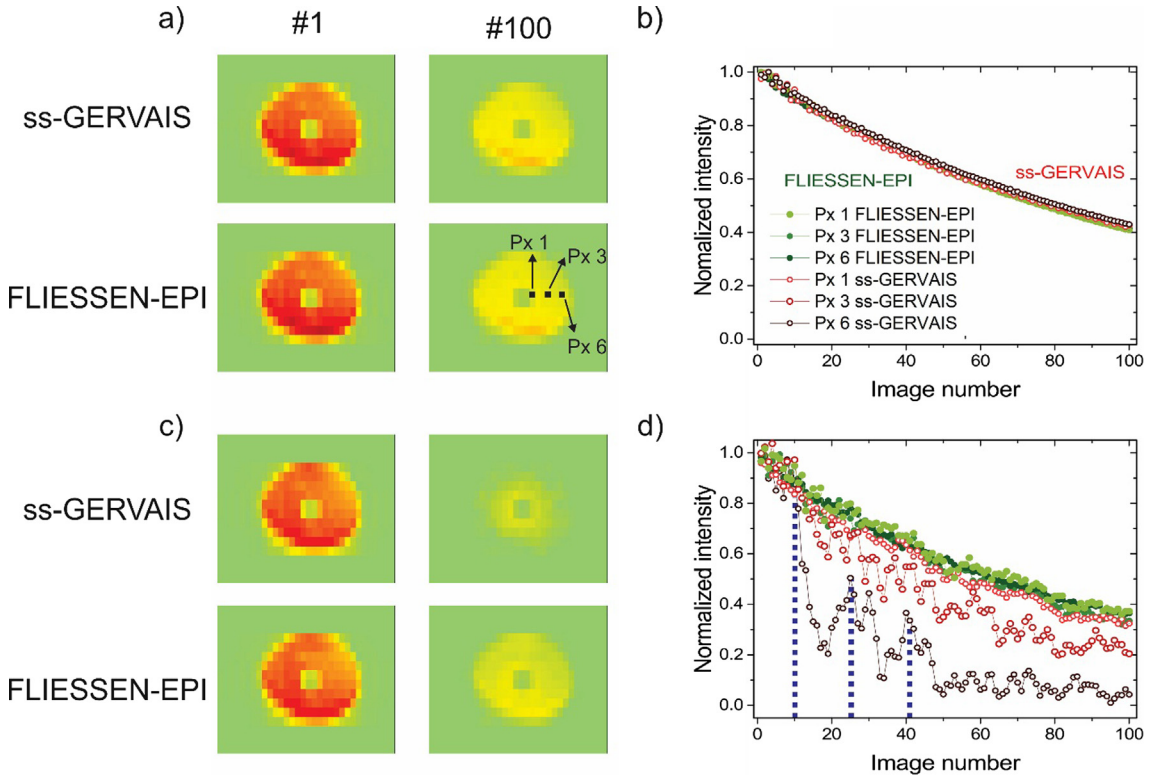

Fig. 2. (a) Comparison of the signal intensity for images 1 and 100 (FOV = 25 × 25 mm^2 and resolution of 781 × 1560 μm^2) acquired with ss-GERVAIS and FLIESSEN-EPI pulse sequences without motion and (c) with the Couette cell rotating at 2rps. (b) Normalized signal intensities for three representative pixels, Px 1 close to the inner cylinder, Px 3 in the central region, and Px 6 close to the outer cylinder for static and (d) rotating conditions.

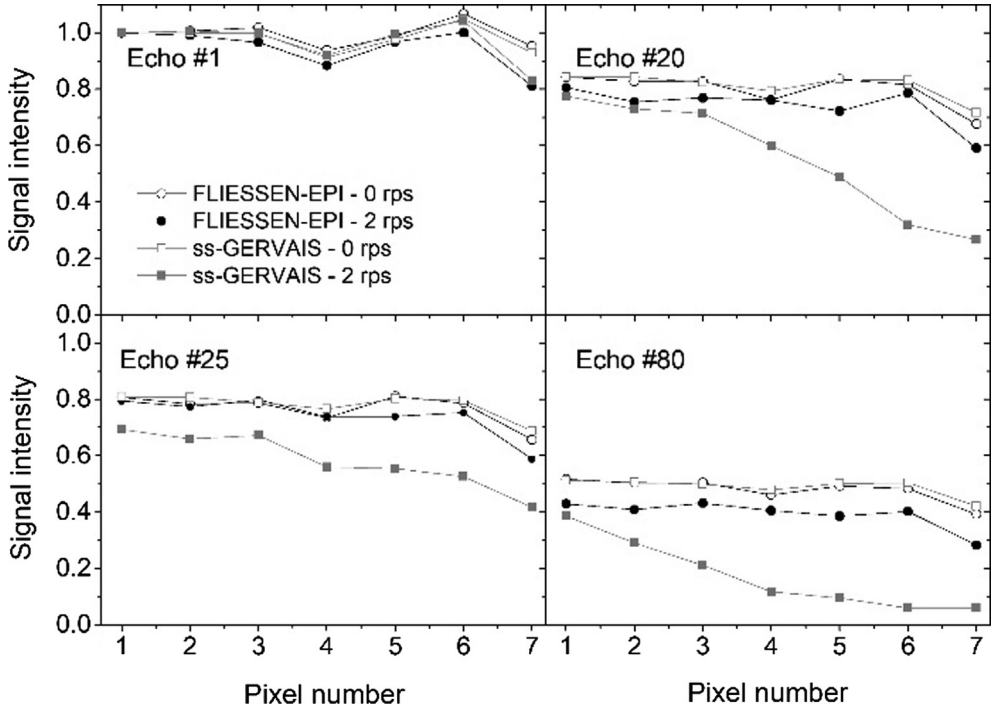

Fig. 3. Signal intensities of the seven pixels marked in Fig. 2 plotted for four different echoes along the echo train, corresponding to echo times of 16 ms, 320 ms, 400 ms, and 1280 ms, respectively. Open symbols refer to pixels of images acquired with FLIESSEN-EPI and ss-GERVAIS with a static Couette cell, while solid symbols refer to a 2 rps rotation frequency. The velocities are 19.6 mm/s for Px 1, 29.4 mm/s for Px2, 39.3 mm/s for Px 3, 49.1 mm/s for Px 4, 58.9 mm/s for Px 5, and 68.7 mm/s for Px 6.

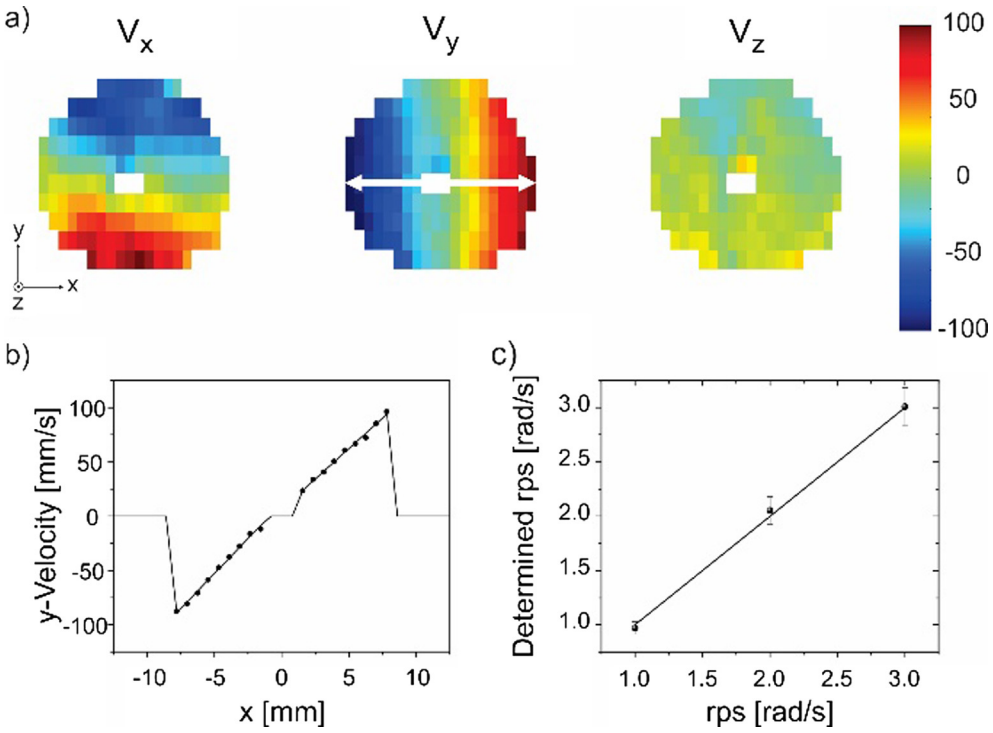

Fig. 4. (a) Velocity component maps along the three orthogonal directions measured by the FLIESSEN-EPI sequence for water confined in a Couette cell where inner and outer cylinders co-rotate at 2 rps. (b) 1D velocity profiles along the x-axis extracted from the *y*-velocity maps (direction marked as a white solid line on the V_y map). As expected, the velocity of the pixels along the x-axis increases linearly with the radius. (c) Rotational frequency (rps) calculated from the experiments.

have a much lower signal intensity than the rest, as that volume is shared by water and the cell material (see Fig. 2a).

3.3. Velocity encoding during long imaging trains

The study of transient phenomena requires the use of rapid acquisition techniques able to accurately map the velocity in the system in real time. To achieve this, we incorporated the concept of phase rewinding after the acquisition of each image in the FLIESSEN-EPI sequence presented in this work. To update the velocity encoding at each echo, two inverse pairs of bipolar gradients are applied. The first one is applied before the acquisition of the image to encode the velocity information, and the second one is applied after the acquisition of the image to remove the velocity phase encoded by the first one. Although the second pair of bipolar gradients refocuses the velocity phase shift inscribed by the first pair, a residual phase due to the acceleration of molecules remains and is carried over to the acquisition of the next echo. For our particular setup, 100 images were acquired. During this time the signal decays to approximately one-third of its initial value. The limiting factor to acquire a large number of images with FLIESSEN-EPI is T_2.

Twenty sets of 5 images were acquired in a single excitation experiment taking a total acquisition time of 1.6 s. During this time the sample was rotating continuously at a constant rotation rate of 2 rps. Five profiles along the x-axis extracted from the *y*-velocity maps at different times along the sequence are shown in Fig. 5a. The velocity profiles remain constant within experimental error as the acquisition of the velocity maps progress during the echo train. The average standard deviation for the velocity maps acquired at a rotation speed of 2 rps is about 7%. The experiments revealed that the FLIESSEN-EPI sequence is suitable for the measurement of three-component velocity maps at a rate of 12.5 frames per second, with a tolerable accumulation of errors for this rotation speed. In order to account for velocity errors, the *y*-velocities encoded in a finite volume element close to the outer wall along the x-axis was simulated for a rotational speed of 2 rps (Fig. 5b), following the description given in Section 2.3. The velocity V_y was calculated as a function of the time during the pulse sequence for the volume element whose position is $x = r_o$ and $y = 0$ and it was normalized to the maximum calculated value. As this is a simulation the only expected source of errors comes from the acceleration, which causes imperfect phase removal at the end of each echo time. During the evolution of the sequence, the signal at the particular pixel of interest generates from voxels with different starting points and different trajectories. As the molecules rotate in a periodic motion inside the cell, the acceleration is a periodic function too, so the phase errors accumulated during the sequence will add and subtract cancelling each other as the maps are acquired. In this way, oscillatory errors are observed. We defined as ε the peak to peak velocity error (shown by the dashed lines in Fig. 5b) and plotted ε as a function of the rotational speed in Fig. 5c. The result shows that ε grows with the applied rotation rate due to the increasing impact of acceleration, which is not compensated by this sequence. For the present setup we found that if an error of about 5% is tolerated then the maximum velocities that the sequence can correctly map can go up to 100 mm/s.

3.4. Flow dynamics during rotations start-up

We start by studying the transient dynamics for the rotation start-up of distilled water inside the co-rotating Couette cell. In all experiments, the engine start was triggered by the NMR console to a value of 2 rps, and a variable delay was used before the determination of a single set of three-component velocity maps, comprising the acquisition of five images. The experimental results are compared to numerical flow simulations. In this way, the data

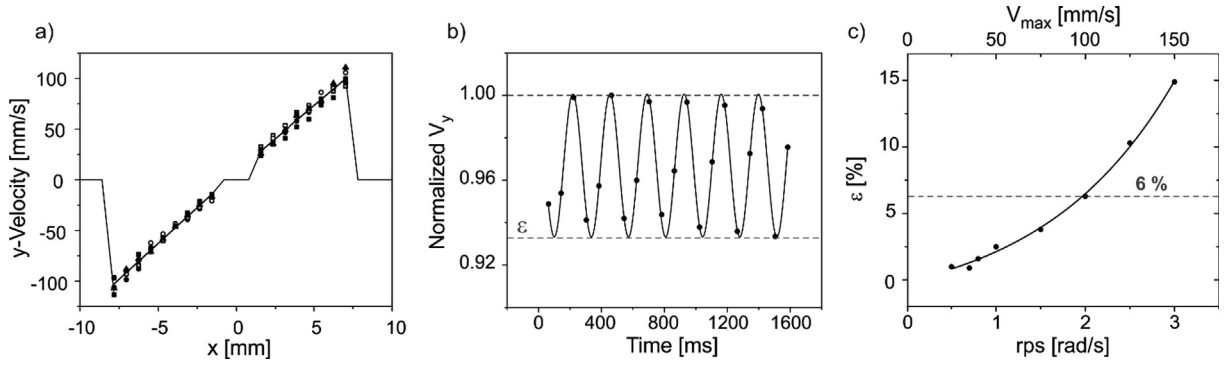

Fig. 5. (a) Velocity profiles extracted from the velocity maps encoded along the *y*-direction at different times during the sequence: 64 ms (solid squares), 384 ms (empty squares), 784 ms (solid circles), 1184 ms (empty circles) and 1584 ms (solid triangles) for a rotation speed of 2 rps. (b) Simulation of the velocity of the volume element closest to the exterior wall of the Couette cell (Px 6), normalized to its maximum velocity, for 2 rps, as a function of the elapsed time during the proposed pulse sequence. (c) The percentage error in the simulated velocity as a function of the applied rotational frequency and the theoretical maximum velocity V_{max} for different rotation speeds, ranging from 0.5 to 3 rps.

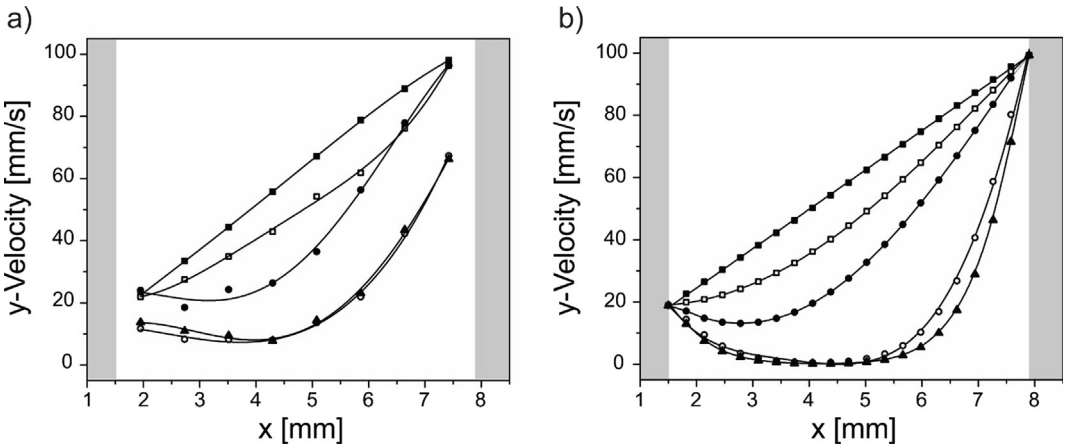

Fig. 6. (a) Experimental and (b) simulated y-velocity profiles for positive values of x position, after the start-up of the motor rotations for different experiments with varying waiting times: 0.8 s (solid triangles), 1 s (empty circles), 3 s (solid circles), 5 s (empty squares) and 12 s (solid squares). The grey areas represent the cell walls.

in Fig. 6, which show half of the cell, are the result of five independent experiments. Flow profiles obtained with the FLIESSEN-EPI experiments are shown in Fig. 6a, where a steady state is accomplished after 12 s; the grey areas represent the inner and outer cell walls. Fig. 6b shows the results obtained with numerical flow simulations as described in Section 2.4, which is in excellent agreement with the experimental data. The following fluid properties were used: kinematic viscosity $\nu = 1 \times 10^{-6}$ m^2/s and $\rho = 1000 \frac{\text{kg}}{\text{m}^3}$. For short delays, on the order of hundreds of milliseconds, the start-up impulse gives rise to a growing velocity of the fluid in contact with the Couette-cell walls. A stationary linear velocity distribution is reached after several seconds. It must be kept in mind that the ability of EPI-based sequences to produce images in just tens of milliseconds comes at the expense of spatial resolution. It can be observed that for the voxel corresponding to the minimum radius, the velocity is not accurately described until the first second. Similar results were obtained by Davies et al. [48], where a steady state was reached after a 5 s delay time, in which a Couette cell of smaller dimensions was employed.

3.5. Flow dynamics during rotations turn-down. Viscosity determination.

We now turn our attention to the study of the response to the cessation of rotations. As the characteristic time of a deceleration experiment is on the order of two seconds, the FLIESSEN-EPI sequence is a suitable tool to study this process in a single-shot experiment. Measurements of 100 images, generating 20 three-component velocity maps were carried out, with a total observation time of 1.6 s. In the first stage, distilled water was employed. After turning on the engine, the sample was sheared for 5 s before the deceleration experiments were carried out. As in the previous experiments, the engine turn-on and shut-down were controlled by the NMR console ensuring the synchronization of image acquisition with the engine shut down. In order to reduce mechanical instabilities, the rotations were turned off with a ramp of 3.3 rps/s. Experimental results are shown in Fig. 7a and numerical simulations in Fig. 7b. Similar to the start-up of rotations, the liquid in contact with the cylinders is the first to respond and stops its movement immediately, while the water in the cell's center continues moving up to 1.6 s after the cylinder rotations have stopped. Good agreement between simulated and experimental data is observed, demonstrating the capability of this technique to obtain valuable information about transient behavior, in a single-shot measurement.

One of the main methods used to obtain information on solute-solvent interactions is viscometry. The particular thermodynamic and physical properties of water/alcohol mixtures are mainly due to the internal solution structure. When dissolved, alcohol molecules locally disrupt the tetrahedral water structure, resulting in a growth of the viscosity of the water/alcohol mixtures. Water

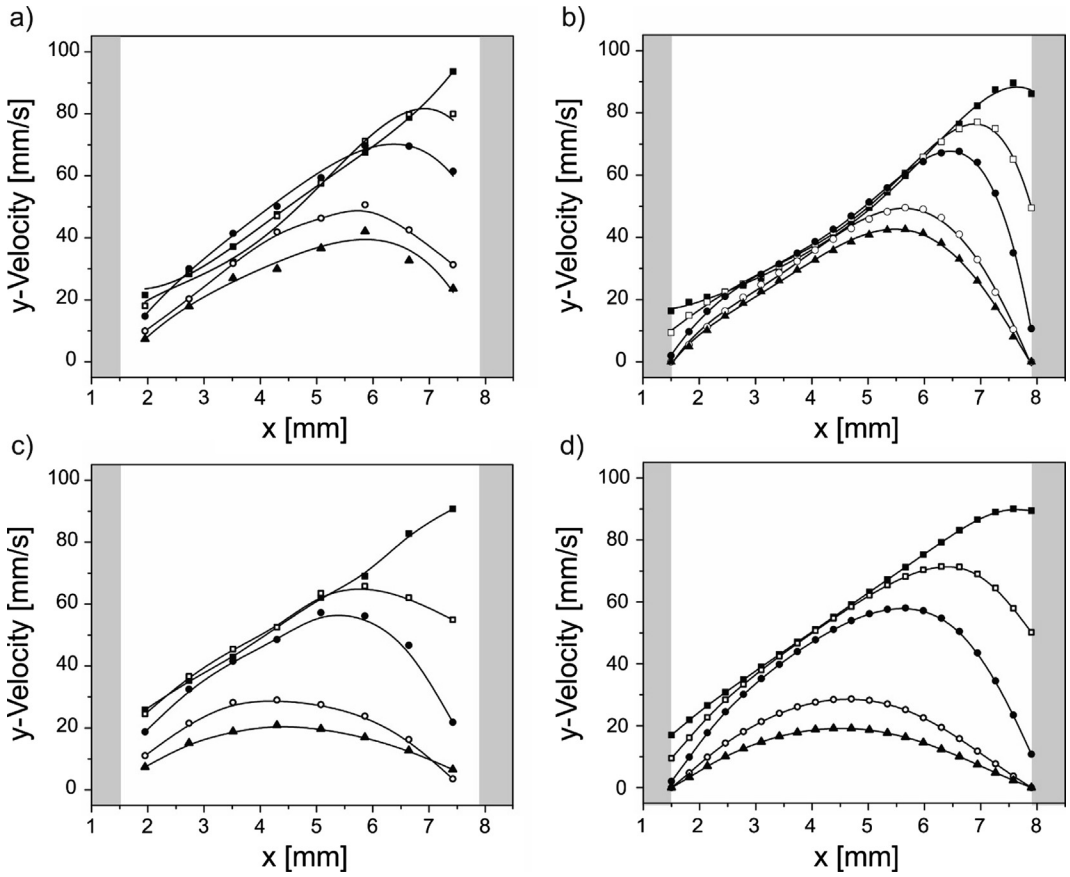

Fig. 7. (a) Experimental and (b) simulated y-velocity profiles for water during the shut-down of the motor rotations at different times during the pulse-sequence acquisition: 64 ms (solid squares), 304 ms (empty squares), 544 ms (solid circles), 1184 ms (empty circles) and 1584 ms (solid triangles). (c) Experimental and (d) simulated velocity profiles in the *y*-direction for the 2-propanol aqueous solution during the shut-down of the motor rotations at different times during the pulse sequence acquisition: 72 ms (solid squares), 342 ms (empty squares), 522 ms (solid circles), 1242 ms (empty circles) and 1602 ms (solid triangles).

molecules tend to organize around alcohol through hydrogen bonds, forming fairly regular cages [30,31]. 2-propanol was recently found to have a greater influence on the water viscosity as a function of alcohol concentration than ethanol [31]. In order to show that the proposed technique can be also used for the indirect measurement of the viscosity, a 2-propanol aqueous solution of 52.7% mol and 82.5% volume concentration was employed. The dynamics after turning down the rotations were studied through the acquisition of 100 images, resulting in 20 three-component velocity maps, with a total observation time of 1.8 s. Fig. 7c reports the experimental results, where the velocity profiles show the expected deceleration patterns, with a faster decrease near the wall. The maximum velocity for the water/2-propanol mixture 1.6 s after the stopping the motor rotations is about 20 mm/s, while water shows a velocity of approximately 45 mm/s at the same time. This is due to the increase in the viscosity when alcohol is dissolved in water.

For a similar 2-propanol aqueous solution, Kuchuk et al. [31] reported a dynamic viscosity of approximately $\eta = 3.2\text{x}10^{-6}$ Pa.s, and a density value of ρ =850 kg/m^3 for 80% of 2-propanol volume concentration, resulting in a kinematic viscosity of $v = 3.8 \times 10^{-6}$ m^2/s. Numerical simulations for a fluid with a kinematic viscosity $v = 3.8 \times 10^{-6}$ m^2/s and $\rho = 850\,\frac{\text{kg}}{\text{m}^3}$ are shown in Fig. 7d. The residuals of the difference between experimental and simulated data were minimized, rendering the reported value of kinematic viscosity, with an error lower than 15%. The dependence of the simulation results on the fluid density proved to be very low. The water and alcohol measurements were compared by plotting the maximum velocity of each profile as a function of time (Fig. 8) for experimental and simulated data. The difference in the velocity decay between both fluids is clearly observed through the change in the slope of the maximum velocities. Further analysis and optimization of the fitting routine and experimental protocol to opti-

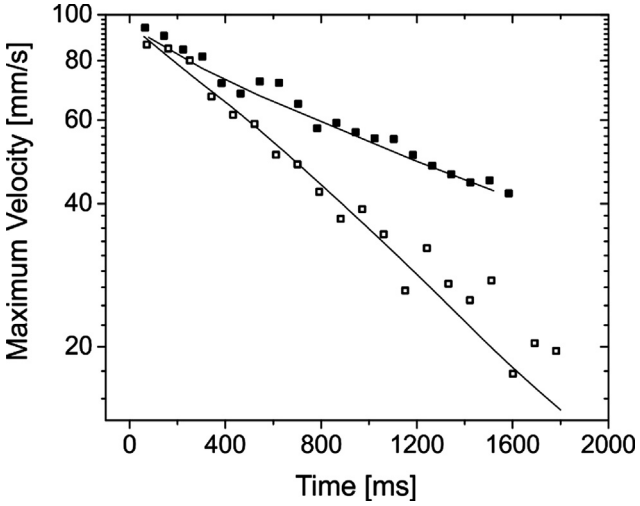

Fig. 8. Maximum velocity as a function of time for water (solid squares) and a 2-propanol aqueous solution (empty squares). The solid lines correspond to the maximum velocities obtained with numerical simulations. Excellent agreement between experimental and simulated data is observed for both fluids.

mize the field of flow, maximum initial velocities and other relevant parameters is beyond the scope of this work and will be reported elsewhere.

4. Conclusions

In this work, we presented the FLIESSEN-EPI sequence and demonstrated its use for acquiring velocity maps in transient states. Two opposite pairs of velocity encoding bipolar gradient bracket the spatial encoding in an EPI sequence, in order to minimize the residual motion-induced phase prior to the following refocusing pulse. By refreshing the velocity encoding in each echo, long trains of echoes could be acquired. In this work, we were able to record transient velocities with up to 100 images, comprising a span of 1.6 s. Additionally, with the aid of numerical simulations, we showed that the system response can be accurately measured to determine the viscosity of a mixture of water/alcohol. This tool, in combination with diffusion and relaxation experiments, may prove very useful to fully characterize liquid mixtures with a single experimental setup.

Acknowledgements

We would like to acknowledge the financial support from CONICET (PIP-11112201301007460O), SeCyT-UNC and ANPCYT (PICT-2014-1295).

References

[1] P.T. Callaghan, Translational Dynamics and Magnetic Resonance: Principles of Pulsed Gradient Spin Echo NMR, Oxford University Press, Oxford, 2011.
[2] S. Stapf, S.-I. Han, NMR Imaging in Chemical Engineering, John Wiley & Sons, 2006.
[3] F. Dorn, F. Niedermeyer, A. Balasso, D. Liepsch, T. Liebig, The effect of stents on intra-aneurysmal hemodynamics: In vitro evaluation of a pulsatile sidewall aneurysm using laser Doppler anemometry, Neuroradiology 53 (2011) 267–272.
[4] C.J. Dimitriou, L. Casanellas, T.J. Ober, G.H. McKinley, Rheo-PIV of a shear-banding wormlike micellar solution under large amplitude oscillatory shear, Rheol. Acta. 51 (2012) 395–411.
[5] M. Nemri, S. Charton, E. Climent, Mixing and axial dispersion in Taylor-Couette flows: the effect of the flow regime, Chem. Eng. Sci. 139 (2016) 109–124.
[6] T. Gallot, C. Perge, V. Grenard, M.-A.A. Fardin, N. Taberlet, S. Manneville, Ultrafast ultrasonic imaging coupled to rheometry: Principle and illustration, Rev. Sci. Instrum. 84 (2013) 045107.
[7] J. Lauri, J. Czajkowski, R. Myllylä, T. Fabritius, Measuring flow dynamics in a microfluidic chip using optical coherence tomography with 1μm axial resolution, Flow Meas. Instrum. 43 (2015) 1–5.
[8] L.F. Gladden, Nuclear magnetic resonance in chemical engineering: principles and applications, Chem. Eng. Sci. 49 (1994) 3339–3408.
[9] E. Fukushima, Nuclear magnetic resonance as a tool to study flow, Annu. Rev. Fluid Mech. 31 (1999) 95–123.
[10] M.D. Mantle, A.J. Sederman, Dynamic MRI in chemical process and reaction engineering, Prog. Nucl. Magn. Reson. Spectrosc. 43 (2003) 3–60.
[11] L.F. Gladden, A.J. Sederman, Recent advances in flow MRI, J. Magn. Reson. 229 (2013) 2–11.
[12] A. Amar, B. Blümich, F. Casanova, Rapid multiphase flow dynamics mapped by single-shot MRI velocimetry, Chem. Phys. Chem. 11 (2010) 2630–2638.
[13] S. Kuczera, P. Galvosas, Advances and artefact suppression in RARE-velocimetry for flow with curved streamlines, J. Magn. Reson. 259 (2015) 135–145.
[14] A.B. Tayler, D.J. Holland, A.J. Sederman, L.F. Gladden, Exploring the origins of turbulence in multiphase flow using compressed sensing MRI, Phys. Rev. Lett. 108 (2012) 264505.
[15] P.R. Moran, A flow velocity zeugmatographic interlace for NMR imaging in humans, Magn. Reson. Imaging 1 (1982) 197–203.
[16] D.N. Firmin, R.H. Klipstein, G.L. Hounsfield, M.P. Paley, D.B. Longmore, Echo-planar high-resolution flow velocity mapping, Magn. Reson. Med. 12 (1989) 316–327.
[17] P. Mansfield, Multi-planar image formation using NMR spin echoes, J. Phys. C Solid State Phys. 10 (1977) L55–L58.
[18] A.M. Howseman, M.K. Stehling, B. Chapman, R. Coxon, R. Turner, R.J. Ordidge, M.G. Cawley, P. Glover, P. Mansfield, R.E. Coupland, Improvements in snap-shot nuclear magnetic resonance imaging, Br. J. Radiol. 61 (1988) 822–828.
[19] K. Kose, One-shot velocity mapping using multiple spin-echo EPI and its application to turbulent flow, J. Magn. Reson. 92 (1991) 631–635.
[20] K. Kose, NMR imaging of turbulent structure in a transitional pipe flow, J. Phys. D. Appl. Phys. 23 (1990) 981.
[21] K. Kose, Instantaneous flow-distribution measurements of the equilibrium turbulent region in a circular pipe using ultrafast NMR imaging, Phys. Rev. A 44 (1991) 2495.
[22] K. Kose, Visualization of local shearing motion in turbulent fluids using echo-planar imaging, J. Magn. Reson. 96 (1992) 596–603.
[23] J.C. Gatenby, J.C. Gore, Echo-planar-imaging studies of turbulent flow, J. Magn. Reson. - Ser. A 121 (1996) 193–200.
[24] A.J. Sederman, M.D. Mantle, C. Buckley, L.F. Gladden, MRI technique for measurement of velocity vectors, acceleration, and autocorrelation functions in turbulent flow, J. Magn. Reson. 166 (2004) 182–189.
[25] A.B. Tayler, A.J. Sederman, B. Newling, M.D. Mantle, L.F. Gladden, "Snap-shot" velocity vector mapping using echo-planar imaging, J. Magn. Reson. 204 (2010) 266–272.
[26] S. Ahola, J. Perlo, F. Casanova, S. Stapf, B. Blümich, Multiecho sequence for velocity imaging in inhomogeneous rf fields, J. Magn. Reson. 182 (2006) 143–151.
[27] T.I. Brox, B. Douglass, P. Galvosas, J.R. Brown, Observations of the influence of Taylor-Couette geometry on the onset of shear-banding in surfactant wormlike micelles, J. Rheol. (N. Y. N. Y) 60 (2016) 973–982.
[28] N.J. Hayden, J. Diebold, G. Noyes, Phase behavior of chlorinated solvent+ water + alcohol mixtures with application to alcohol flushing, J. Chem. Eng. Data 44 (1999) 1085–1090.
[29] U. Buhvestov, F. Rived, C. Ràfols, E. Bosch, M. Rosés, Solute–solvent and solvent–solvent interactions in binary solvent mixtures. Part 7. Comparison of the enhancement of the water structure in alcohol–water mixtures measured by solvatochromic indicators, J. Phys. Org. Chem. 11 (1998) 185–192.
[30] E.J.W. Wensink, A.C. Hoffmann, P.J. van Maaren, D. van der Spoel, Dynamic properties of water/alcohol mixtures studied by computer simulation, J. Chem. Phys. 119 (2003) 7308–7317.
[31] V.I. Kuchuk, I.Y. Shirokova, E.V. Golikova, Physicochemical properties of water-alcohol mixtures of a homological series of lower aliphatic alcohols, Glas. Phys. Chem. 38 (2012) 460–465.
[32] K.Y. Lee, Viscosity of high-alcohol content fuel blends with water: Subsurface contaminant transport implications, J. Hazard. Mater. 160 (2008) 94–99.
[33] G. Kacar, G. de With, Hydrogen bonding in DPD: application to low molecular weight alcohol–water mixtures, Phys. Chem. Chem. Phys. 18 (2016) 9554–9560.
[34] M.Z. Jora, M.V.C. Cardoso, E. Sabadini, Correlation between viscosity, diffusion coefficient and spin-spin relaxation rate in 1 H NMR of water-alcohols solutions, J. Mol. Liq. 238 (2017) 341–346.
[35] Z.J. Derlacki, A.J. Easteal, A.V.J. Edge, L.A. Woolf, Z. Roksandic, Diffusion coefficients of methanol and water and the mutual diffusion coefficient in methanol-water solutions at 278 and 298 K, J. Phys. Chem. 89 (1985) 5318–5322.
[36] J. McGregor, R. Li, J.A. Zeitler, C. D'Agostino, J.H.P.P. Collins, M.D. Mantle, H. Manyar, J.D. Holbrey, M. Falkowska, T.G.A.A. Youngs, C. Hardacre, E.H. Stitt, L.F. Gladden, Structure and dynamics of aqueous 2-propanol: A THz-TDS, NMR and neutron diffraction study, Phys. Chem. Chem. Phys. 17 (2015) 30481–30491.
[37] P.A. Artola, A. Raihane, C. Crauste-Thibierge, D. Merlet, M. Emo, C. Alba-Simionesco, B. Rousseau, Limit of miscibility and nanophase separation in associated mixtures, J. Phys. Chem. B. 117 (2013) 9718–9727.
[38] M.R. Serial, M.I. Velasco, E.V. Silletta, F.M. Zanotto, S.A. Dassie, R.H. Acosta, Flow-pattern characterization of biphasic electrochemical cells by magnetic resonance imaging under forced hydrodynamic conditions, ChemPhysChem 18 (2017) 3469–3477.
[39] L.D. Landau, E.M. Lifshitz, Fluid Mechanics: Landau and Lifshitz: Course of Theoretical Physics, Elsevier, 2013.
[40] X. He, L.-S. Luo, Theory of the lattice Boltzmann method: From the Boltzmann equation to the lattice Boltzmann equation, Phys. Rev. E 56 (1997) 6811.
[41] S. Succi, The Lattice Boltzmann Equation: for Fluid Dynamics and Beyond, Oxford University Press, Oxford, 2001.
[42] D.A. Wolf-Gladrow, Lattice-gas Cellular Automata and Lattice Boltzmann Models: An Introduction, Springer Science & Business Media, 2000.
[43] S. Harris, An introduction to the theory of the Boltzmann equation, Courier Corporation, 2004.
[44] Y. Sone, Molecular Gas Dynamics: Theory, Techniques, and Applications, Springer Science & Business Media, 2007.
[45] D. D'Humières, I. Ginzburg, M. Krafczyk, P. Lallemand, L.-S. Luo, Multiple-Relaxation-Time Lattice Boltzmann Models in 3D Multiple-relaxation-time lattice Boltzmann, Philos. Trans. R. Soc. London A Math. Phys. Eng. Sci. 360 (2002) 437–451.
[46] P. Lallemand, L.-S. Luo, Theory of the lattice Boltzmann method: Dispersion, dissipation, isotropy, Galilean invariance, and stability, Phys. Rev. E 61 (2000) 6546.
[47] I. Ginzburg, D. d'Humières, Multireflection boundary conditions for lattice Boltzmann models, Phys. Rev. E 68 (2003) 66614.
[48] C.J. Davies, A.J. Sederman, C.J. Pipe, G.H. McKinley, L.F. Gladden, M.L. Johns, Rapid measurement of transient velocity evolution using GERVAIS, J. Magn. Reson. 202 (2010) 93–101.